

On the recombination centers of iron-gallium pairs in Ga-doped silicon

Tine Uberg Nærland,^{1,a)} Simone Bernardini,¹ Halvard Haug,² Sigbjørn Grini,³ Lasse Vines,³ Nathan Stoddard,⁴ and Mariana Bertoni¹

¹Ira A. Fulton Schools of Engineering, Arizona State University, 650 E. Tyler Mall, Tempe, Arizona 85287, USA

²Department for Solar Energy, Institute for Energy Technology, Instituttveien 18, 2007 Kjeller, Norway

³Center for Materials Science and Nanotechnology, Department of Physics, University of Oslo, P.O. Box 1048 Blindern, N-0316 Oslo, Norway

⁴Solar World Industries America, 25300 NW Evergreen Rd, Hillsboro, Oregon 97124, USA

(Received 10 March 2017; accepted 15 August 2017; published online 28 August 2017)

Gallium (Ga) doped silicon (Si) is becoming a relevant player in solar cell manufacturing thanks to its demonstrated low light-induced degradation, yet little is known about Ga-related recombination centers. In this paper, we study iron (Fe)-related recombination centers in as-grown, high quality, directionally solidified, monocrystalline Ga-doped Si. While no defect states could be detected by deep level transient spectroscopy, lifetime spectroscopy analysis shows that the minority carrier lifetime in as-grown wafers is dominated by low levels of FeGa related defect complexes. FeGa pairs have earlier been shown to occur in two different structural configurations. Herein, we show that in terms of recombination strength, the orthorhombic pair-configuration is dominant over the trigonal pair-configuration for FeGa. Furthermore, the defect energy level in the band gap for the **orthorhombic defect center is determined to be $E_V + 0.09$ eV**, and the capture cross-section ratio of the same defect center is determined to be 220. *Published by AIP Publishing.* [<http://dx.doi.org/10.1063/1.5000358>]

I. INTRODUCTION

The ultimate task in solar cell research is to improve efficiency while decreasing the overall cost per Watt produced. Currently, crystalline silicon (c-Si) modules represent 90% of the global annual market and will most likely continue to be the dominant technology also in the years to come.¹ High-efficiency cells on crucible-grown single crystal Czochralski (Cz) silicon and cast multicrystalline (mc) silicon both have the potential for reducing this cost, but boron-doped p-type Cz-Si, unfortunately, suffers from the formation of a metastable defect under carrier injection. This defect reduces the bulk lifetime and causes industrial screen-printed solar cells to decrease from 1 to 1.5% in absolute efficiency (or 7 to 10% relative efficiency).^{2,3} The phenomenon is often referred to as light-induced degradation (LID) and is increasingly becoming a problem for more inexpensive silicon materials, like mc-Si and monolike-Si, as the quality of these keeps on improving.

Many efforts have been made to eliminate, or at least minimize, LID.^{4–6} Since both boron dopants and oxygen impurities are incorporated during the crystal growth, many of the strategies to overcome the LID effect involve changes to the crystal growth process. The strategy behind these efforts has been to lower the concentration of either oxygen or boron. Some of the proposed approaches include **Magnetically Confined Czochralski (MCZ) growth to reduce the oxygen content**,⁶ the use of float zone substrate to eliminate the oxygen from the crystal,⁶ the use of a higher resistivity target to lower the concentration of boron,⁷ and finally the switch to n-type substrates⁸ to all-in-all eradicate the boron content. For a long

time, researchers have **proposed Ga as an alternative p-type dopant**, with the benefit over n-type silicon that the mobility of its minority carriers is three times higher than for phosphorous doped material. Glunz *et al.*⁵ have compared Ga-doped Cz-Si (Ga-Si) to boron-doped Cz-Si with $7.5 \times 10^{-17} \text{ cm}^{-3}$ of oxygen content showing the direct correlation of degradation to the B-O pairs. Not only does Ga-Si with a significant interstitial oxygen concentration show no degradation, but it also has been shown to give a high carrier lifetime.^{9–11} A recent research also shows that **Ga-Si is significantly less affected by the not so well understood “Light and elevated temperature induced degradation” (LeTID) mechanism**.¹² Ga is not commonly used as a dopant in crystalline silicon (c-Si) solar cells due to its low segregation coefficient, which causes large resistivity variations in the silicon ingot after solidification. Lately, however, new methods for overcoming this problem in Ga-doped c-Si have been developed, enabling low resistivity variation over the crystal height.

All-in-all, Ga-doped Cz-Si shows promising performance as a starting material for photovoltaic applications, and the potential of this type of material is highlighted by the fact that minority carrier lifetimes up to 1.7 ms have been reported, comparable to p-type float zone.¹³ Replacing B with Ga as a p-type dopant thus suppresses LID originated by B-O related defects, but little is known so far regarding the interaction of Ga with iron, oxygen, and carbon.^{14,15}

In p-type Si, interstitial iron is known to significantly reduce the effective minority carrier lifetime.¹⁶ In boron doped Si, the interstitial iron will form a complex with substitutional boron that acts as an effective lifetime killer. These defects can in some cases be identified by their smaller degree of injection dependence compared with iron in the unpaired interstitial state, Fe_i. By illuminating or heating the sample, it

^{a)}Author to whom correspondence should be addressed: tine.uberg@gmail.com

is possible to switch between the two states. In the case of B-doped silicon, 95% of all Fe is bound in the associated state of FeB pairs at room temperature and $[B] > 10^{14} \text{ cm}^{-3}$, whereas at temperatures above approximately 200 °C and $[B] < 10^{16} \text{ cm}^{-3}$ most Fe is dissociated into interstitial sites.¹⁷ In this paper, we investigate if Ga-doped silicon with iron contamination shares the same characteristics as B-doped silicon and what is the typical signature of the lifetime reducing defect centers in Ga-Si. The manuscript starts with an overview of the properties of Fe acceptors in silicon and continues with the experimental details of the work. In Sec. IV, we present the results from injection- and temperature-dependent lifetime spectroscopy (TIDLS), and further on, we present our results and analysis of the Fe_i and FeGa lifetime crossover point with temperature, enabling determination of the capture cross section for holes and electrons at FeGa defects. Lastly, we present our results from attempting to probe the Fe_i and FeGa recombination centers by deep level transient spectroscopy (DLTS).

II. PAIRING OF INTERSTITIAL IRON WITH SHALLOW ACCEPTORS

It has been previously shown that Fe atoms introduced to the silicon crystal occupy tetrahedral interstitial sites¹⁸ and behave as donors.¹⁹ Fe atoms are electrically neutral (Fe^0) in n-type silicon and positively charged (Fe^+) in p-type silicon. Due to the high diffusivity of interstitial Fe^+ even at room temperature, positively charged Fe^+ forms neutral Fe-acceptor pairs with negatively charged substitutional acceptor impurities such as boron, aluminum, gallium, and indium.^{20,21} The driving force for the formation of iron-acceptor pairs is the electrostatic attraction between the positively charged interstitial iron (Fe_i^+) and the negatively charged substitutional acceptor ($\text{As}^- = \text{B}^-, \text{Al}^-, \text{Ga}^-, \text{and In}^-$). The equilibrium of the defect reaction



depends on the temperature and the acceptor concentration.¹⁷

Electron spin resonance (ESR) studies have clarified that Fe-acceptor pairs have two structural configurations: trigonal and orthorhombic symmetry.^{18,22,23} The pairs with trigonal symmetry have Fe atoms occupying the first nearest-neighbor interstitial sites adjacent to acceptors along the $\langle 111 \rangle$ direction. The pairs with orthorhombic symmetry have Fe atoms that occupy the second nearest-neighbor interstitial sites adjacent to acceptors along the $\langle 100 \rangle$ direction (see Fig. 1).^{23–25}

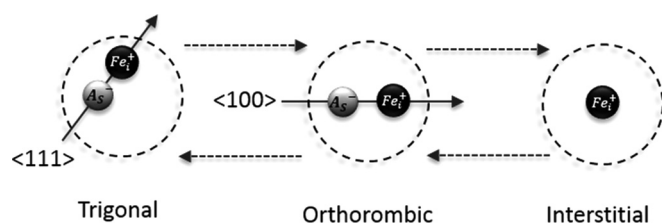


FIG. 1. The three states schematically shown in this figure are the states in which the iron-acceptor will occur in silicon doped with boron, gallium, aluminum, and indium. The state will change upon illumination, heating, or carrier injection.²⁴

Both of these configurational pairs are observed experimentally in Fe-contaminated specimens in the cases of B-, Al-, Ga-, and In-doped samples but with some variations. For example, the orthorhombic FeB pair is only detected when the sample is illuminated or injected with minority carriers at temperatures below 150 K,²⁶ and so in FeB-materials, the only configuration that can be seen at room temperature is the trigonal configuration. In In-Si material, on the other hand, it is the orthorhombic configuration that is found to be stable at room temperature.²⁷ As pointed out by Zhao *et al.*,²⁸ there is an overall trend that when shifting to an acceptor with a higher atomic number, the stability of iron-acceptor pairs changes from the trigonal configuration to the orthorhombic.

Except for one paper,¹⁵ all previous reports on the energy level and the capture cross section of electrons and holes for FeGa defects derive from DLTS studies at low temperatures (an overview of literature results are presented in Table I). In the one paper presenting injection dependent lifetime spectroscopy (IDLs) data at room temperature,¹⁵ the underlying assumption is that the trigonal configuration of the FeGa is predominant. Hence, a coexistence of the orthorhombic defect center would not be recognized but rather lead to an underestimation of E_t and k -values for the trigonal FeGa defect center. The work presented herein is based on the TIDLS analysis of Fe-containing Ga-doped Si making no assumption regarding the configurational nature of the defects—both the trigonal and orthorhombic defect center can occur simultaneously. We observe that similar to In-Si material, there is a predominance of the orthorhombic center in Ga-Si. This indicates that the orthorhombic defect configuration is the most stable configuration in Fe-containing Ga-Si at room temperature.

III. EXPERIMENTAL DETAILS

Five directionally solidified $12.5 \times 12.5 \text{ cm}^2$ Ga-doped Si wafers with a thickness of 180 μm and a doping concentration of $1.2 \times 10^{16} \text{ cm}^{-3}$ were used for this study. The growth technique is a contactless bulk crystal growth method for producing single crystal ingots as described in Ref. 36 where liquid silicon is continuously fed onto a crystalline silicon seed layer in order to maintain the same resistivity throughout the ingot height. Only material from the non-seed part of the ingot is used in this investigation. The process, called NeoGrowth,³⁷ has no containment crucible and thus no foreign contact during crystal growth, providing capability for very high purity ingots. As in most silicon crystal growth, iron is the chief quality-limiting impurity despite the availability of contact-diffusion. The major route of iron incorporation is through gas-phase deposition of iron onto the solidified material, where the iron source is evaporation from other parts of the hot zone.

The interstitial oxygen content of these wafers, as determined by infrared absorption, was in the range of $1.3\text{--}1.5 \times 10^{17} \text{ cm}^{-3}$, whereas the substitutional carbon content was in the range of $2.5\text{--}3.5 \times 10^{17} \text{ cm}^{-3}$. Prior to the lifetime measurements, the wafers were cleaned with Piranha, RCA-B, and BOE solutions and thereafter received a 50 nm double side passivation by plasma-enhanced chemical-vapor-deposited

TABLE I. Literature values for Fe_i and FeGa recombination centers.

Defect d = donor	Author	Reference	Characterization method	$E_t^{\text{Fe}_i}$ (eV)	Axis orientation	$\sigma_p^{\text{Fe}_i}$ (cm ²)	$\sigma_n^{\text{Fe}_i}$ (cm ²)	k_{Fe_i}
Fe _i (d)	Istratov <i>et al.</i>	16 ^a	DLT, Hall, PhCap, ESR	$E_V + 0.38$		7.0×10^{-17}	4.0×10^{-14}	571
Fe _i (d)	Macdonald <i>et al.</i>	29	IDLS	$E_V + 0.48$		7.0×10^{-17}	1.3×10^{-14}	186
Fe _i (d)	Rein and Glunz	30	IDLS/TIDLS	$E_V + 0.39$		7.0×10^{-17}	3.6×10^{-15}	51
Fe-Ga (d)	Graff and Pieper	19	DLTS	$E_V + 0.25$	$\langle 111 \rangle$			
Fe-Ga (d)	Schmidt and Macdonald	15	IDLS	$E_V + 0.20$	$\langle 111 \rangle$	2.0×10^{-14}	4.0×10^{-14}	2
Fe-Ga (d)	Ciszek <i>et al.</i>	32	DLTS	$E_V + 0.21$	$\langle 111 \rangle$	6.0×10^{-15}		
Fe-Ga (d)	Dahl <i>et al.</i>	33	DLTS	$E_V + 0.26$	$\langle 111 \rangle$			
Fe-Ga (d)	Lemke	17	DLTS	$E_V + 0.24$	$\langle 111 \rangle$	3.0×10^{-15}		
Fe-Ga (d)	Wunstel and Wagner	20	DLTS	$E_V + 0.24$	$\langle 111 \rangle$	2.0×10^{-14}		
Fe-Ga (d)	Chantre	27	DLTS	$E_V + 0.24$	$\langle 111 \rangle$			
Fe-Ga (d)	Yoon <i>et al.</i>	34	DLTS	$E_V + 0.23$	$\langle 111 \rangle$	5.5×10^{-15}		
Fe-Ga (d)	Beljacowa <i>et al.</i>	35	DLTS	$E_V + 0.24$	$\langle 111 \rangle$	2.0×10^{-14}		
Fe-Ga (d)	Ciszek <i>et al.</i>	32	DLTS	$E_V + 0.10$	$\langle 100 \rangle$	3.0×10^{-16}		
Fe-Ga (d)	Yoon <i>et al.</i>	34	DLTS	$E_V + 0.13$	$\langle 100 \rangle$	2.5×10^{-14}		
Fe-Ga (d)	Graff	31 ^a	DLTS	$E_V + 0.14$	$\langle 100 \rangle$			
Fe-Ga (d)	Chantre	27	DLTS	$E_V + 0.14$	$\langle 100 \rangle$			
Fe-Ga (d)	Beljacowa <i>et al.</i>	35	DLTS	$E_V + 0.15$	$\langle 100 \rangle$	1.5×10^{-14}		

^aValues are an average from results presented in a range of articles.

(PECVD) hydrogenated amorphous silicon (a-Si:H). A postannealing of the a-Si:H-passivated samples was performed for 30 min at 280 °C in a muffle furnace with air. The a-Si:H-passivation provides an excellent and stable level of surface passivation with a surface recombination velocity below 3 cm/s.³⁸

To measure the injection level-dependent effective carrier lifetimes, we apply the contactless quasi-steady-state photoconductance (QSSPC) technique. The Sinton WCT-120TS tool used in this work is equipped with a heating stage which allows for acquiring the lifetime vs. injection curves in a range of temperatures going from room temperature to 230 °C. Details on the technique can be found in Refs. 39 and 40.

To dissociate the FeGa pairs, a 50 W/cm² halogen lamp as in Ref. 19 was used *in situ* on the QSSPC stage. The dissociation rate of the iron-acceptor pair is a function of the doping concentration,¹⁷ and with our rather high doping concentration of 1.2×10^{16} cm⁻³, we found that already after 3 min, at room temperature, there were no further changes in the minority carrier lifetime. From this, we made the assumption that after 3 min, the amount of dissociated pairs had reached saturation. Pair splitting (dissociation) by this method has the benefit that the sample can reside on the Sinton tester for all measurements without being moved back and forth, thus avoiding any source of error related to sample positioning. Problems related to lamp-associated heating of the stage are eluded with TIDLS.

To determine the crossover-point of the dark and light soaked lifetime curves presented in Sec. IV D, we measured the samples after storage in the dark for >24 h. To make sure that the samples were not exposed to any light prior to the flash of the lifetime measurement, the samples were dark-stored prior to every temperature assessment of the FeGa-Fe_i lifetime crossover-point. Several gray filters in front of the lamp were engaged in order to be able to measure minority carrier lifetime at low injection levels.

The DLTS measurements were carried out using a refined version of the set-up described in Ref. 41, on samples with the Schottky contact consisting of a stack of 50 and 150 nm of titanium and aluminium deposited by e-beam evaporation, respectively. The temperature was scanned between 30 and 300 K, and the DLTS signal was extracted using a lock-in weighting function with six rate windows from 20 ms⁻¹ to 640 ms⁻¹, applying a reverse bias of 10 V and a filling pulse of 10 V with 50 ms duration. Minority carrier traps were investigated by minority carrier transient spectroscopy (MCTS) using a forward biasing light emitting diode (LED) with a peak wavelength of 940 nm, providing backside optical excitation of the charge carriers.

IV. RESULTS AND DISCUSSION

A. Minority carrier lifetime measurements

In this paper, we have studied industrially manufactured Ga-doped silicon. No Fe was deliberately introduced to the material, but in typical directionally solidified silicon, some degree of Fe contamination is practically impossible to avoid.^{37,42} Graphite and insulation parts can, for example, be significant sources of iron, circulated by evaporation. In the wafers used for this study, a dramatic increase in carrier lifetime was observed after phosphorous diffusion³⁹ suggesting the presence of a mobile metal contaminant as the lifetime limiting source. Although other metal impurities expected to be influenced by gettering could in principle also account for the lifetime reduction, we show elsewhere⁴³ that it is reasonable to assume that Fe is the main lifetime-dominating contaminant in these wafers.

It was already shown in Ref. 43 that Ga-doped silicon is not prone to light-induced degradation. As mentioned in Sec. III, we did measure an oxygen concentration $>1 \times 10^{17}$ cm⁻³ in this material, but we see no traces of oxygen related defects with heating or illuminating the material. Upon cycling

heating and cool-down with varying time, we acquire the exact same lifetime curves at all stages, indicating no influence by oxygen-related thermal donors. Formation of thermal donors has other time-scales than iron-related defects as oxygen in its interstitial form has a significantly lower mobility than iron. Formation of thermal donors is also reported to be occurring at higher temperatures than 235 °C.⁴⁴

As discussed in Sec. III, the relative populations of Fe–B pairs and Fe_i can be varied by exposing the samples to light and subsequently storing the wafers in the dark prior to lifetime measurements. Figure 2 shows the minority carrier lifetime as a function of excess carrier density (Δn) for an as-grown, Ga-doped wafer. Measurements are shown for three different states of the sample: after storage in the dark for 24 h (black circles), after light soaking (red triangles), and after different times of storage following the light soaking (gray diamonds). From Fig. 2, we can see that after 30 min of storage subsequent to light soaking, the lifetime has recovered its initial value prior to light soaking. The rate at which this recovery occurs depends on the doping concentration and the temperature.¹⁷

As reported elsewhere,⁴³ it is not possible to obtain a good fit to any of the data in Fig. 2 using a Shockley-Read-Hall (SRH) model with a single defect level. This suggests that in the Ga-doped Si material with a doping level of $1.2 \times 10^{16} \text{ cm}^{-3}$, the FeGa complexes never reach 100% association nor dissociation, assuming that we have no other lifetime dominating defects present. However, by altering the relative fractions of Fe_i and FeGa defects, using defect-parameters reported in Refs. 15 and 29, we can reconstruct the dark stored, the light-soaked, and all the intermediate lifetime curves while maintaining the same total iron concentration. The lack of complete dissociation is in line with measurements performed on B-Si with a similar doping level⁴⁶ and is believed to be due

to the very fast and exponential re-association rate of the dopant element. A fast enough acquisition of the lifetime, after the illumination is turned off, is practically unattainable. The reason for incomplete association seems to be related to an increase in repulsion between the acceptor atom and Fe by the electron shells of Ga being a comparatively larger atom than B.²⁸

Figure 3 shows lifetime curves measured in the dark stored state and the light-soaked state at temperatures ranging from 21 °C to 235 °C. The curves measured in the completely light-soaked state (red triangles) are varying very little with temperature, which indicates the presence of a close to mid band gap (deep) defect state, whereas the lifetime curves in the dark stored state (black dots) have a large temperature dependence, with increasing lifetime at higher temperatures, consistent with what is expected from a defect with a shallow energy level.⁴⁷ The lifetime curves in the dark stored state in Fig. 3 are steadily increasing up until 221 °C for injections of $5 \times 10^{15} \text{ cm}^{-3}$ and above. This is in contrast to the comprehensively studied FeB - Fe_i system,^{30,46} where the FeB complex is completely dissociated and the dark stored state lifetime curve is already overlapping with the light-soaked state curve at 150 °C. This indicates that FeGa complexes are more energetically stable than FeB. This point will be further discussed in Sec. IV B.

In the Ga-Si material under investigation, the FeGa complexes are never completely associated nor dissociated. Because of the very different nature of these defects, however—one being deep and one being shallow—we can exploit the fact that the two defects will dominate in different parts of the injection range: the Fe_i defect will prevail at low injections, and the FeGa defect will dominate at high injections. In Sec. IV B on defect parameter contour mapping (DPCM), we have consequently used only parts of the lifetime curves to

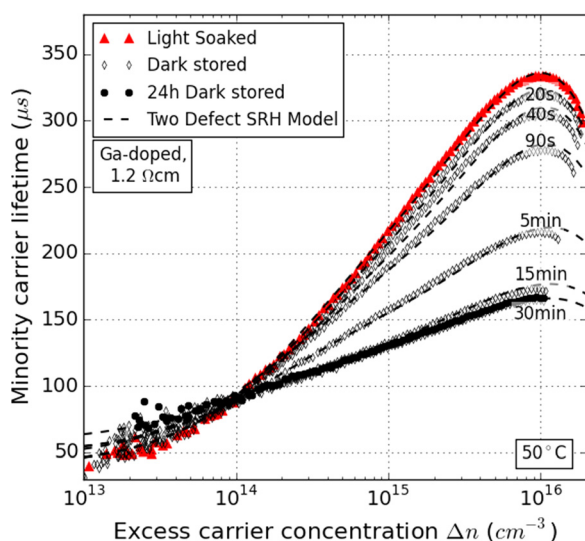


FIG. 2. Lifetime measurement example from wafer 1 after storage in the dark, after light soaking, and at different times of dark storage subsequent to the illumination. All the curves can be observed to pivot through a point at $\sim 10^{14} \text{ cm}^{-3}$, which corresponds to the Fe_i-FeGa crossover-point.⁴⁵ The curves are fitted with a two defect SRH model using Fe_i parameters from Ref. 29 and FeGa parameters from Ref. 15 maintaining a fixed total concentration of Fe.

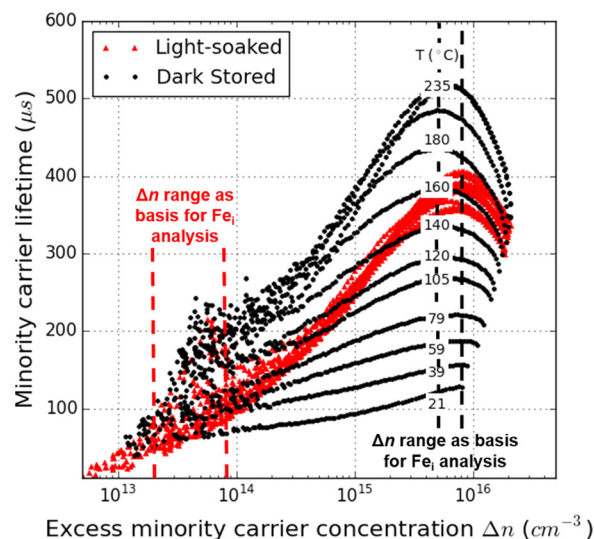


FIG. 3. Minority carrier lifetime as a function of excess carrier concentration at different temperatures, after storage in the dark, and after light soaking, performed on wafer 2. In the light-soaked state, the lifetime is measured for the same temperatures as indicated for the dark stored state and has slightly an increasing trend with temperature throughout the injection range. The higher noise level in Fig. 3 compared to Fig. 2 is caused by the measurement settings in Fig. 3, which are set to meet the large temperature range employed which induces some more noise at the lower temperatures.

analyze the Fe_i and the FeGa defect, respectively. The ranges applied for analysis are indicated in Fig. 3.

B. Defect parameter contour mapping (DPCM)

Temperature and injection dependent lifetime spectroscopy (TIDLS) has been recognized as capable of providing extremely high sensitivity to electrically active defects and to add valuable insight into defects not accessible by any other characterization technique.^{47,48} In this section, we use our recently developed defect parameter contour mapping (DPCM) method to analyze TIDLS data and determine the characteristics of the most dominating recombination center in (i) the completely light-soaked state and (ii) the dark stored state of the Fe-contaminated Ga-doped Si material. The method is based on using the SRH theory to calculate the fit quality of a simulated curve to a measured curve, for a given range of values for the defect energy level (E_t) and the capture cross-section ratio (k) (see Appendix A for a detailed description). For every E_t - k combination, the time constants τ_{p0} and τ_{n0} are varied until a best fit of the experimental data is obtained. The quality of the fit, represented by lighter color in the contour plot, is determined by calculating an *average residual value*:

$$\text{Average Residual Value} = \sum_{j=1}^m \left(\left(\sum_{i=1}^n \frac{|\tau_{\text{measured},j} - \tau_{\text{model},j}|}{\tau_{\text{measured},j}} \right) / n \right) / m, \quad (2)$$

where n is the number of injection level values and m is the number of temperatures taken into account. Two significant advantages of using DPCM to determine electronic properties of defects are that the method does not rely on highly uncertain estimations of the contaminant concentration from diffusion calculations and that we do not simplify the SRH-equation for high or low injection range conditions with the uncertainty that this introduces. A more detailed description of the method can be found in Ref. 48.

In Fig. 4(a), the TIDLS-DPCM plot for the completely light-soaked state is shown. The plot shows the area where a good fit to the measured data can be obtained, represented by the bright region, corresponding to $E_t^{\text{Fe}_i} = 0.43_{-0.03}^{+0.03}$ eV and $k = 327_{-93}^{+112}$. The error is estimated by determining the extension of E_t and k values giving rise to a 5% relative increase in the residual value plus the experimental standard deviation (1% for the E_t - and 19% for the k -value) determined by repeating the measurement 5 times. Previously reported values of E_t and k for Fe_i are given in Table I, and it can be seen that the Fe_i parameters reported herein fall within the range reported by Macdonald *et al.*²⁹ and Istratov *et al.*¹⁶

The corresponding DPCM map for the lifetime curves in the dark stored state is shown in Fig. 4(b). The map reveals that the dominating recombination center is best described by an E_t^{FeGa} -value of $E_V + 0.09_{-0.03}^{+0.01}$ eV and a k -value of 217_{-96}^{+162} . The trigonal and the orthorhombic donor defect configuration of FeGa have earlier been reported in the range of $E_t^{\text{FeGa}^{\text{trig}}} = E_V + (0.20-0.25)$ eV for the trigonal defect center and $E_t^{\text{FeGa}^{\text{orth}}} = E_V + (0.10-0.15)$ eV for the orthorhombic defect center (see Table I).

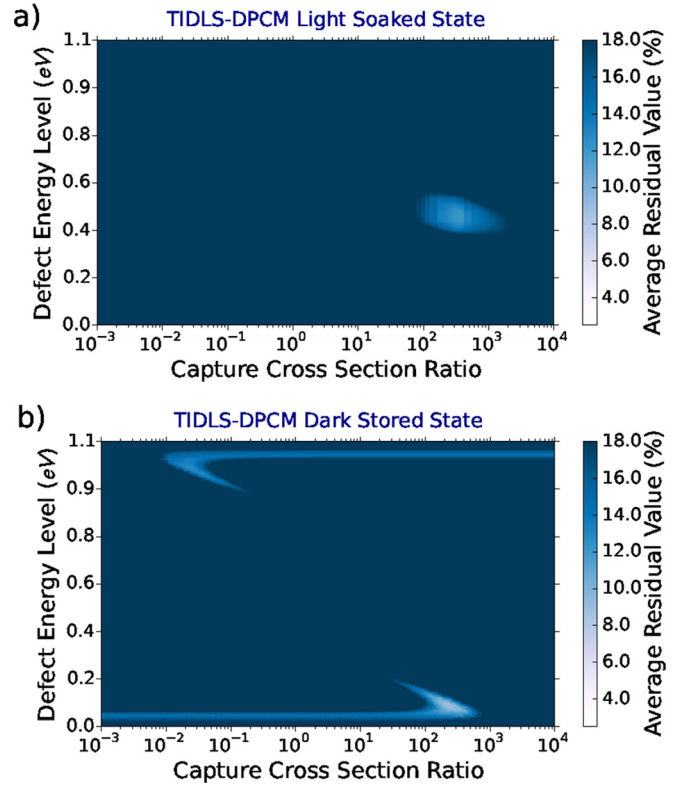


FIG. 4. (a) DPCM plot of TIDLS data taken in the light-soaked state (lifetime curve shown in Fig. 3). Injection levels in the range of $2-8 \times 10^{13} \text{ cm}^{-3}$ are considered to ensure recombination from Fe_i only. $E_t^{\text{Fe}_i}$ determined to $E_V + 0.43_{-0.03}^{+0.03}$ and k to 327_{-93}^{+112} , respectively. (b) DPCM plot of TIDLS data for lifetime curves taken in the dark stored state from raw data in Fig. 3. Injection levels in the range of $2-8 \times 10^{13} \text{ cm}^{-3}$ are considered to ensure recombination from FeGa only. E_t^{FeGa} and k are for the orthorhombic defect configuration, which is determined to $E_V + 0.09_{-0.03}^{+0.01}$ and 217_{-96}^{+162} , respectively. In both plots, the τ_{p0} range utilized for the fitting is approximately $1 \times 10^{-11} - 2 \times 10^{-2} \text{ s}$.

In contrast to the hypothesis that the trigonal configuration is expected to act as the dominating recombination center in Ga-Si,¹⁵ our results indicates that, in line with In-Si, it is the orthorhombic FeGa configuration (FeGa^{orth}) that dominates the lifetime.

As described by Kimerling and Benton,⁴⁹ the stable configuration switches from $\langle 111 \rangle$ -trigonal to $\langle 100 \rangle$ -orthorhombic for Fe_iA_s pairs going from B_s to In_s and is related to an increase in the repulsion between A_s and Fe_i when the atomic number increases. The minimum energy potential difference (ΔE) associated with the switch between the two configurations also decreases with the change in the charge state of the Fe_i-ion (in the FeA_s complex) going from a double positive state (Fe⁺⁺), via a single positive state (Fe⁺) to a neutral state (Fe⁰).

Calculations for the ΔE associated with the switch from trigonal to orthorhombic configuration for FeGa are calculated to change from $0.15 \rightarrow 0.03 \rightarrow -0.06$ eV throughout the Fe⁺⁺ \rightarrow Fe⁺ \rightarrow Fe⁰ transition, respectively.²⁸ Hence, in the neutral charge state of the complex, there is a higher probability of being in the orthorhombic configuration than in the trigonal. The defect can switch back and forth between charge state A and charge state B by a mechanism such as the Fermi level shift caused by temperature variation. The

acceptor defect level associated with the $(\text{Fe}^{+/0}\text{Ga}^-)^{-/0}$ is estimated to be approximately 0.15 eV below the conduction band,²⁸ and hence it cannot be expected to be filled with electrons by the temperature associated Fermi-level shift for a p-type material.

The defect level of $(\text{Fe}^{++/+}\text{Ga}^-)^{0/+}$ is, however, reported to be in the range of $E_v + (0.20\text{--}0.25)$ (see Table I) and is more likely to be subject to a charge state change by temperature associated Fermi-level shift at temperatures above 300 K. We find it, therefore, likely that the FeGa complex occurs in its single positive state at the temperatures under study. We acknowledge that theoretical calculations show that the trigonal configuration has a slight predominance in this charge state;²⁸ however, the ΔE associated with this switch is very low. In light of our experimental results, we propose that, as for In-Si, it is the orthorhombic and not the trigonal configuration that is the most stable defect center in iron contaminated Ga-Si at room temperature. It should be noted that in our experiments, we did not see any increment of the fit quality for the orthorhombic defect with increased temperature ($T > 100^\circ\text{C}$). Hence, there does not seem to be any increase in the charge state change in $(\text{Fe}^{++/+}\text{Ga}^-)^{0/+}$ causing a configurational change, at temperatures between 100 and 230°C .

C. Defect parameter contour mapping (DPCM) with simulated lifetime curves

In the past, fitting lifetime curves for FeGa with Shockley-Read-Hall (SRH) statistics has given good results with E_t -values in the area $E_v + (0.20\text{--}0.25)$ eV and k -values from 2 to 3. A root for misconception, which we see from our TIDLS-DPCM plots, is, however, the existence of almost equally good

areas of fit close to the valence band at $E_t = 0.24$ eV and $E_t = 0.09$ eV when fitting FeGa curves. This is something that can easily cause misinterpretation both in IDLS and in TIDLS analyses. In Figs. 5(a) and 5(c), we have simulated lifetime curves, using the theory in Appendix A, over a temperature range of $25\text{--}230^\circ\text{C}$ for (a) a defect with $E_t = 0.24$ eV, $k = 3$ and (b) a defect with $E_t = 0.09$ eV, $k = 236$. τ_{p0} is in both cases set to $500\ \mu\text{s}$. The corresponding DPCM plots resulting from fitting these simulated lifetime curves are given in b) and c), respectively. The white areas correspond to good fits taking only the room temperature lifetime curve into account. This is what is commonly known as an injection dependent lifetime spectroscopy (IDLS) approach. As can be observed from the IDLS-DPCM plots, there are a vast amount of combinations of E_t 's and k 's that give an equally good fit for both of the simulated defects. From the white areas in Figs. 5(b) and 5(c), we can observe that the E_t and k combination of the trigonal defect center ($E_t = 0.24$ and $k = 3$) and the E_t and k combination of the orthorhombic defect center ($E_t = 0.09$ and $k = 236$) have equally good fits, regardless of which defect is simulated.

If we add the temperature to the analysis, i.e., TIDLS (maroon areas represent good fit), we can see that the areas of good fit are narrowed down significantly. However, there are still multiple regions in the DPCM plot, which produce an equally good fit. What we observe is a symmetry effect of these two pairs of E_t and k values in TIDLS. Looking at the similar simulated lifetime curves that these two defects produce (a) and (c), the coinciding of fit is not surprising. If care is not taken to analyze the whole range of E_t and k values, TIDLS analysis may therefore potentially lead to non-unique solutions and erroneous results.

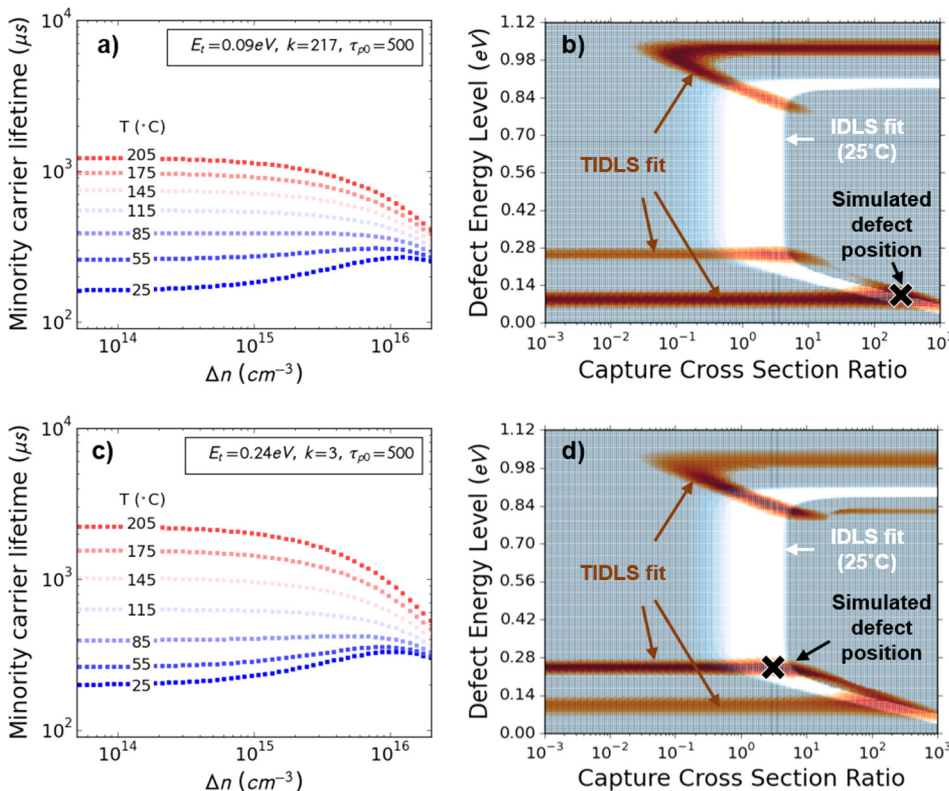


FIG. 5. Simulated lifetime curves at temperatures ranging from 25 to 205°C for a pure orthorhombic defect (a) and a pure trigonal defect (c). The corresponding IDLS- and TIDLS-DPCM analyses of the curves are given in (b) and (d), respectively. Regardless of the defect analyzed, the DPCM plots show that there is also a fit of the data misleadingly pointing to another defect in the lower band gap half. This can easily lead to misconception of the E_t and k values for the FeGa defect. In the DPCM plots, lifetime values for an injection range of $5 \times 10^{13}\text{--}1 \times 10^{16}\text{ cm}^{-3}$ are analyzed.

With the data set that we have available in this work, we can determine that the lower donor level has a significantly better fit to our experimentally collected raw data than the upper donor level, even when taking the symmetry-effect discussed above into account. Hence, we confirm that the orthorhombic donor level is the dominating state level of the FeGa complex.

D. Arrhenius plot of Fe_i and FeGa lifetime curve crossover-point

As a complimentary measurement to TIDLS-DPCM, the characteristic crossover-point of the carrier lifetime curves before and after light soaking has been measured as a function of temperature. This method may provide additional information on the electronic properties of the FeGa-complex. A typical crossover-point can be observed in Fig. 2 where the Fe_i defect and the FeGa defect exhibit the higher recombination activity under low-level injection (LLI) and high-level injection (HLI), respectively.

Consequently, dissociation of FeGa pairs leads to a lifetime decrease under LLI conditions and a lifetime increase under HLI conditions. At the crossover-point (Δn_{COP}) of the two lifetime curves, however, carrier lifetime remains unchanged upon defect transformation, as the recombination activity of the FeGa and the Fe_i defect is the same in this particular point. In lifetime terms, this is described by the following equation:

$$\begin{aligned} \text{At } \Delta n_{\text{COP}} : \frac{1}{\tau^{\text{FeGa}^{100}}(\text{as})} + \frac{1}{\tau^{\text{Fe}_i}(\text{as})} \\ = \frac{1}{\tau^{\text{FeGa}^{100}}(\text{dis})} + \frac{1}{\tau^{\text{Fe}_i}(\text{dis})}. \end{aligned} \quad (3)$$

Previous attempts to probe the crossover point of Fe_i and FeGa lifetime curves have been performed on Czochralski grown silicon, which naturally contains a great amount of oxygen. As a consequence, the lower injection ranges were influenced by carrier trapping, and no crossover point was detectable. Our material is grown by directional solidification and is therefore less subjected to oxygen contamination. As can be seen in Figs. 2 and 3, the Fe_i -FeGa lifetime curve crossover points can be clearly extracted. The crossover-point is a function of doping and temperature and will increase with increasing temperature.⁵⁰ At room-temperature, the crossover-point of the FeGa-material is $\sim 3 \times 10^{13} \text{ cm}^{-3}$, close to the detection limit of our QSSPC setup, and the number of points is scarcer and accordingly noisier. For clarity, in Fig. 2 we therefore show the crossover-point at 50 °C.

For the Arrhenius plot study described in this section, a corresponding crossover-point was assessed for every tenth degree in a temperature range from 23 to 140 °C. By applying a similar approach as Birkholz *et al.*,⁵⁰ where the acceptor energy level and capture cross sections of FeGa pairs can be determined independently of the total iron concentration, we have plotted the crossover point (Δn_{COP}) for temperatures ranging from 23 to 140 °C in an Arrhenius plot (see Fig. 6). The slope of the linear fit of the curve in Fig. 6 yields E_t^{FeGa} , whereas σ_p^{FeGa} is determined from the offset. These two are

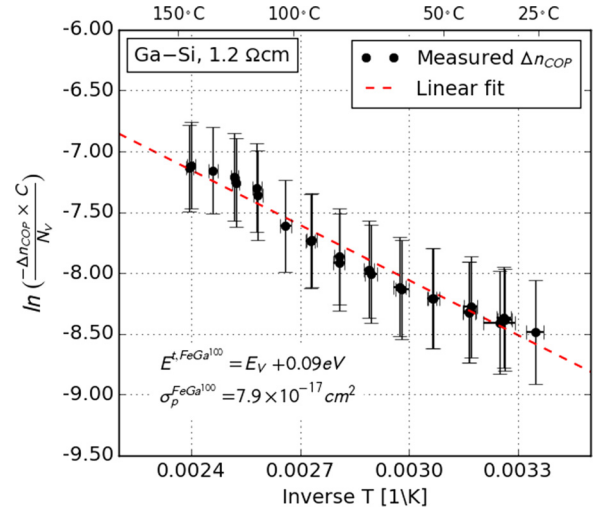


FIG. 6. Arrhenius plot of the Δn_{COP} measured for a temperature range of 23–140 °C. The slope of the curve gives E_t^{FeGa} . The error bars were determined from a combination of the uncertainty in the temperature (3%), the wafer thickness (2%), and calibration (4%). This figure includes data from wafers 2 to 5.

dependent parameters and in determining one of them we need, information on the other. The theory and equations employed in this calculation are given in Appendix B. Assuming known values for $\sigma_n^{\text{Fe}_i}$ and $\sigma_p^{\text{Fe}_i}$,²⁹ see Table I, forcing the slope of the linear fit to equal the defect energy of FeGa^{100} $E_t^{\text{FeGa}} = E_v + 0.09 \text{ eV}$ determined from fig. b), and keeping the capture cross section ratio fixed to the k -value of 217, we can calculate $\sigma_n^{\text{FeGa}} = 1.9 \times 10^{-14} \text{ cm}^2$ and $\sigma_p^{\text{FeGa}} = 7.9 \times 10^{-17} \text{ cm}^2$. The σ_n^{FeGa} has not been determined before but the low $\sigma_p^{\text{FeGa}} = 7.9 \times 10^{-17} \text{ cm}^2$ is in line with what Ciszek *et al.* have reported.³² The high σ_n^{FeGa} value can explain why a shallow recombination center like $E_v + 0.09 \text{ eV}$ can be a very efficient recombination center.

As described in Sec. IV C, there is a coinciding fit of the trigonal and the orthorhombic defects with TIDLS-DPCM. Even though we have a better fit for the orthorhombic configuration, we cannot discard the co-existence of the two defects. Inevitably this adds a level of uncertainty to the estimation of σ_p^{FeGa} and σ_n^{FeGa} .

E. Deep level transient spectroscopy (DLTS)

Several studies of Fe-Ga related defect centers have been performed by DLTS in the past^{17,20,32–35} (see Table I) with some of them being capable of probing both the trigonal and the orthorhombic defect center. Two of these studies were performed on material with naturally incorporated Fe from the silicon growth, with one study able to see possibly iron-related defects at $E_v + 0.13 \text{ eV}$ and $E_v + 0.23 \text{ eV}$,³⁴ and the other seeing DLTS peaks that are too broad to isolate individual defects.³³

In this study, we have performed both DLTS and minority carrier transient spectroscopy (MCTS) on a set of Ga-Si wafers with naturally incorporated Fe. In DLTS, the charge emission from majority carrier traps is observed by the application of a filling pulse as stated in Sec. III, while in MCTS the minority carrier traps can be observed by backside

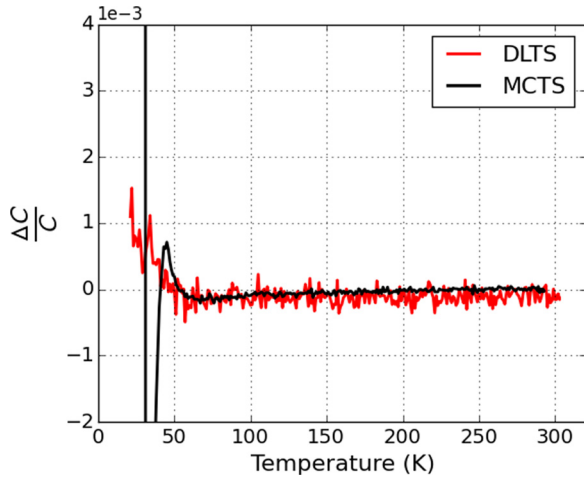


FIG. 7. DLTS and MCTS spectra (one window shown) of $1.2 \times 10^{16} \text{ cm}^{-3}$ doped Ga-Si naturally containing Fe. No defect levels can be deduced. The DLTS and MCTS measurements were performed on wafer 1.

optical excitation above the band gap during the filling pulse. The two methods, therefore, complement each other by, respectively, probing the opposite band gap halves.

In Fig. 7, DLTS and MCTS spectra for one frequency window of the $1.2 \times 10^{16} \text{ cm}^{-3}$ doped Ga-Si material are shown. The Ti-Al stacked Schottky contact produced good rectifying contacts, verified by CV and IV-measurements. However, no defect levels, iron-related or not, could be detected. Hence, with a DLTS/MCTS detection limit of $<N_A/1000$, this sets an upper concentration limit to the iron concentration.

V. CONCLUSION

Due to the performance-limiting effects associated with light-induced degradation commonly observed in boron doped silicon, gallium doped silicon is presently becoming a relevant player in solar cell manufacturing. As in boron-doped silicon, in gallium-doped silicon, interstitial iron is also known to significantly reduce the effective minority carrier lifetime. In this paper, we report on iron (Fe)-related recombination centers in as-grown, high-quality, directionally solidified, mono-crystalline Ga-doped Si. While no defect states could be detected by deep level transient spectroscopy, temperature and injection dependent spectroscopy (TIDLS) analysis by defect parameter contour mapping (DPCM) showed that the minority carrier lifetime in as-grown wafers is dominated by low levels of FeGa pairs with an energy level of 0.09 eV above the valence band and a capture cross section ratio of 220. We attribute this defect to the known orthorhombic configuration of the FeGa complex and simultaneously propose that in Fe-containing Ga-Si at room temperature, it is the orthorhombic configuration that represents the most stable configuration as opposed to the trigonal one.

ACKNOWLEDGMENTS

This project was funded by U.S. Department of Energy's SolarMat II under Contract No. DE-EE0006806.

The authors would like to thank Dr. Mathieu Boccard for help with the surface passivation of the material.

APPENDIX A: MINORITY CARRIER LIFETIME ANALYSIS BY SHOCKLEY READ HALL THEORY

Lifetime measurements obtained by the QSSPC method represent *effective* lifetimes, meaning that they comprise components caused by various recombination mechanisms. It is essential therefore to be aware of which mechanisms occur and what their relative contributions are. In many practical cases, more than one type of SRH center may be present simultaneously. This is also the case for the lifetime curves in Figs. 2 and 3 but since we know that the Fe_i defect exhibits the higher recombination activity under low-level injection and the FeGa defect exhibits the higher recombination activity under high-level injection, we can choose portions of the lifetime curve where we can assume we have a single SRH center manifesting itself. The effective lifetime τ_{eff} is calculated according to Eq. (A1) where $\tau_{\text{intrinsic}}$ is estimated using Richter's model,⁵¹ while τ_{surface} is neglected due to high quality surface passivation (3 cm/s) in combination with moderate effective lifetime in the samples of investigation. More details on the models implemented for $\tau_{\text{intrinsic}}$ can be found in Ref. 48 and references therein

$$\frac{1}{\tau_{\text{eff}}} = \frac{1}{\tau_{\text{SRH}}} + \frac{1}{\tau_{\text{intrinsic}}} + \frac{1}{\tau_{\text{surface}}}. \quad (\text{A1})$$

The lifetime attributed to recombination through defects in a sample with an acceptor (donor) doping concentration $N_A(N_D)$ can be described by τ_{SRH} .^{52,53} The expression given in Eq. (A2) is exemplified for the p-type case. In the defect parameter contour mapping (DPCM) method, we use the SRH equation as it is with no simplifications for deep or shallow levels, at high or low injection levels

$$\tau_{\text{SRH}} = \frac{\tau_{n0}(N_A + p_1 + \Delta n) + \tau_{p0}(n_1 + \Delta n)}{N_A + n_0 + \Delta n}, \quad (\text{A2})$$

where the electron- and hole-capture time constants τ_{n0} and τ_{p0} are related to the defect density N_t , the thermal velocity $v_{\text{th}} = 1.1 \times 10^7 \text{ cm s}^{-1}$ (at $T = 300 \text{ K}$),⁵⁴ and the electron- and hole-capture cross sections σ_n and σ_p via

$$\tau_{p0} = 1/N_t \sigma_p v_{\text{th}}, \quad \text{and} \quad \tau_{n0} = 1/N_t \sigma_n v_{\text{th}} \quad (\text{A3})$$

n_0 is the thermal equilibrium concentration of holes. The k -value is the ratio between the electron- and hole-capture time constants and accordingly also the electron- and hole-capture cross sections given by

$$k = \tau_{p0}/\tau_{n0} = \sigma_n/\sigma_p. \quad (\text{A4})$$

The densities n_1 and p_1 equal the equilibrium electron and hole densities when the defect energy level E_t coincides with the Fermi level

$$p_1 = N_v \exp\left(-\frac{E_t - E_v}{kT}\right) n_1 = N_c \exp\left(-\frac{E_c - E_t}{kT}\right). \quad (\text{A5})$$

Values for the effective densities of states in the conduction and valence band at 300 K are taken as $N_c = 2.86 \times 10^{19} \text{ cm}^{-3}$ and $N_v = 3.10 \times 10^{19} \text{ cm}^{-3}$.⁵⁵

APPENDIX B: ARRHENIUS PLOT FROM CROSSOVER-POINT EQUATIONS

The injection level at which we find the crossover point of the Fe_i -dominating curve and the FeGa dominating curve (Δn_{COP}) with temperature is another piece of information that can reveal insight into the electronic properties of the FeGa complex.

$$\Delta n_{\text{COP}} = - \frac{[p_0 + p_1^{\text{FeGa}} + k^{\text{FeGa}} n_1^{\text{FeGa}}] - (\sigma_n^{\text{FeGa}} / \sigma_n^{\text{Fe}_i}) \times [p_0 + p_1^{\text{Fe}_i} + k^{\text{Fe}_i} n_1^{\text{Fe}_i}]}{[1 + k^{\text{FeGa}}] - (\sigma_n^{\text{FeGa}} / \sigma_n^{\text{Fe}_i}) \times [1 + k^{\text{Fe}_i}]} \quad (\text{B1})$$

The Ga-concentration $p_0 = 1.2 \times 10^{16} \text{ cm}^{-3}$ and we can therefore neglect $n_1^{\text{FeGa}} \approx 10^4 \text{ cm}^{-3}$, $n_1^{\text{Fe}_i} \approx 10^{11} \text{ cm}^{-3}$, and $p_1^{\text{Fe}_i} \approx 10^8 \text{ cm}^{-3}$. Consequently, we can rewrite Eq. (B1) to

$$\Delta n_{\text{COP}} = - \frac{p_1^{\text{FeGa}} + p_0 \left(1 - \left(\frac{\sigma_n^{\text{FeGa}}}{\sigma_n^{\text{Fe}_i}} \right) \right)}{[1 + k^{\text{FeGa}}] - (\sigma_n^{\text{FeGa}} / \sigma_n^{\text{Fe}_i}) \times [1 + k^{\text{Fe}_i}]} \quad (\text{B2})$$

In Refs. 46 and 15, the assumption $\sigma_p^{\text{Fe}_i} \ll \sigma_n^{\text{Fe}_i}$, and σ_n^{FeGa} and σ_p^{FeGa} are made to further simplify the equation. Herein, we have chosen not to make this assumption since the size of $\sigma_n^{\text{Fe}_i}$ still is under debate (see Table I) and the sizes of σ_n^{FeGa} and σ_p^{FeGa} are what we want to determine.

If we now insert Eq. (A5) into Eq. (B2), we can rearrange the equation to make an Arrhenius plot where the slope of the curve is corresponding to $E_t^{\text{FeGa}^{100}}$

$$\ln \left(\frac{\Delta n_{\text{COP}} \times C}{N_v} \right) = - \left(\frac{E_t - E_v}{k} \right) \left(\frac{1}{T} \right), \quad (\text{B3})$$

where

$$C = \left([1 + k^{\text{FeGa}}] - (\sigma_n^{\text{FeGa}} / \sigma_n^{\text{Fe}_i}) \times [1 + k^{\text{Fe}_i}] \right) - p_0 \left(1 - \left(\frac{\sigma_n^{\text{FeGa}}}{\sigma_n^{\text{Fe}_i}} \right) \right). \quad (\text{B4})$$

Equation (B3) is what is employed in the Arrhenius plot in Fig. 6.

In the following, we will show how we use the Δn_{COP} at different temperatures to extract information on the capture cross section of the FeGa^{100} ($\sigma_n^{\text{FeGa}^{100}}$ and $\sigma_p^{\text{FeGa}^{100}}$) assuming the values reported by Macdonald *et al.*²⁹ (see Table I).

The recombination lifetime attributed to the association and dissociation of the FeGa complex in p-type silicon with an acceptor concentration N_A can be described by the standard Shockley-Read-Hall (SRH) theory from Eqs. (A2)–(A5) as in Appendix A.

By inserting (A3)–(A5) into (A2) and solving the third order polynomial as shown in Ref. 50, we end up with

- ⁵S. W. Glunz, S. Rein, and J. Knobloch, in *Proceedings of the 16th European Photovoltaic Solar Energy Conference* (Glasgow, 2000), p. 1070.
- ⁶J. Zhao, A. Wang, and M. A. Green, *Prog. Photovoltaics: Res. Appl.* **7**, 471 (1999).
- ⁷J. Knobloch, S. W. Glunz, D. Biro, W. Warta, E. Schaeffer, and W. Wettling, in *Proceedings of the 25th IEEE Photovoltaic Specialist Conference* (Washington, 1996), p. 405.
- ⁸J. Benick, B. Hoex, G. Dingemans, W. Kessels, A. Richter, M. Hermle, and S. W. Glunz, in *Proceedings of the 24th European Photovoltaic Solar Energy Conference* (Hamburg, Germany, 2009), p. 863.
- ⁹S. W. Glunz, B. Köster, T. Leimenstoll, S. Rein, E. Schäffer, J. Knobloch, and T. Abe, *Prog. Photovoltaics: Res. Appl.* **8**, 237 (2000).
- ¹⁰J. Schmidt, *Solid State Phenom.* **95–96**, 187 (2004).
- ¹¹G. Crabtree, T. L. Jester, C. Fredric, J. Nickerson, V. Meemongkolkiat, and A. Rohatgi, in *Proceedings of the Conference Record of the Thirty-First IEEE Photovoltaic Specialists Conference* (Lake Buena Vista, FL, 2005), p. 935–938.
- ¹²K. Petter, paper presented at the 9th Workshop on Crystalline Silicon Solar Cells, Tempe, Arizona (2016).
- ¹³N. Stoddard, B. Gründig-Wendrock, A. Krause, D. Oriwol, M. Bertoni, T. U. Nærlund, I. Witting, and L. Sylla, *J. Cryst. Growth* **452**, 272–275 (2016).
- ¹⁴A. Khan, M. Yamaguchi, Y. Ohshita, N. Dharmarasu, K. Araki, T. Abe, H. Itoh, T. Ohshima, M. Imaizumi, and S. Matsuda, *J. Appl. Phys.* **90**, 1170 (2001).
- ¹⁵J. Schmidt and D. H. Macdonald, *J. Appl. Phys.* **97**, 113712 (2005).
- ¹⁶A. A. Istratov, H. Hieslmair, and E. R. Weber, *Appl. Phys. A* **69**, 13 (1999).
- ¹⁷H. Lemke, *Phys. Status Solidi A* **64**, 215 (1981).
- ¹⁸H. H. Woodbury and G. W. Ludwig, *Phys. Rev.* **117**, 102 (1960).
- ¹⁹K. Graff and H. Pieper, *J. Electrochem. Soc.* **128**, 669 (1981).
- ²⁰K. Wünnel and P. Wagner, *Appl. Phys. A* **27**, 207 (1982).
- ²¹L. V. C. Assali and J. R. Leite, *Phys. Rev. B* **36**, 1296 (1987).
- ²²G. W. Ludwig and H. H. Woodbury, *Phys. Rev. Lett.* **5**, 98 (1960).
- ²³W. Gehlhoff, P. Emanuelsson, P. Omling, and H. G. Grimmeiss, *Phys. Rev. B* **41**, 8560 (1990).
- ²⁴L. Dobaczewski and L. Surma, in *Proceedings of the XXV International School of Semiconducting Compounds* (Jaszowiec, 1996), p. 613.
- ²⁵H. Takahashi, M. Suezawa, and K. Sumino, *Jpn. J. Appl. Phys., Part 1* **36**, 6807 (1997).
- ²⁶S. Sakauchi, M. Suezawa, K. Sumino, and H. Nakashima, *J. Appl. Phys.* **80**, 6198 (1996).
- ²⁷L. C. K. A. Chantre, *Mater. Sci. Forum* **10–12**, 387 (1986).
- ²⁸S. Zhao, L. V. C. Assali, J. F. Justo, G. H. Gilmer, and L. C. Kimerling, *J. Appl. Phys.* **90**, 2744 (2001).
- ²⁹D. Macdonald, J. Tan, and T. Trupke, *J. Appl. Phys.* **103**, 073710 (2008).

¹Technology Roadmap: Solar Photovoltaic Energy (International Energy Agency, 2014), p. 9.

²H. Hashigami, Y. Itakura, and T. Saitoh, *J. Appl. Phys.* **93**, 4240 (2003).

³M. Sheoran, A. Upadhyaya, and A. Rohatgi, *IEEE Trans. Electron Devices* **53**, 2764 (2006).

⁴N. B. Mason, T. M. Bruton, S. Gledhill, K. C. Heasman, O. Hartley, C. Morilla, and S. Roberts, in *Proceedings of the 19th European PV Solar Energy Conference* (Paris, 2004), p. 620.

- ³⁰S. Rein and S. W. Glunz, *J. Appl. Phys.* **98**, 113711 (2005).
- ³¹K. Graff, *Metal Impurities in Silicon-Device Fabrication* (Springer, 1999), p. 82.
- ³²T. F. Ciszek, G. H. Schwuttke, and K. H. Yang, *J. Cryst. Growth* **46**, 527 (1979).
- ³³E. Hvidsten Dahl, V. Osinniy, K. Friestad, A. Sjøiland, Y. Safir, W. Skorupa, R. Tronstad, and A. Nylandsted Larsen, *Phys. Status Solidi C* **9**, 2017 (2012).
- ³⁴Y. Yoon, Y. Yan, N. P. Ostrom, J. Kim, and G. Rozgonyi, *Appl. Phys. Lett.* **101**, 222107 (2012).
- ³⁵S. Beljakowa, D. Karg, G. Pensl, and J. Schmidt, in *Proceedings of the 19th European Photovoltaic Solar Energy Conference* (Paris, France, 2004), p. 705.
- ³⁶N. Stoddard and W. Von Ammon, "Apparatus and method for the production of ingots," U.S. patent 9,315,917 (2016).
- ³⁷N. Stoddard, J. Russell, E. Hixson, H. She, W. Chester, A. Krause, F. Wolny, M. Bertoni, T. U. Nærland, L. Sylla, and W. von Ammon, "NeoGrowth Silicon: A new high purity, low-oxygen crystal growth technique for photovoltaic substrates," *Prog. Photovoltaics: Res. Appl.* (submitted 2017).
- ³⁸S. Y. Herasimenka, W. J. Dauksher, and S. G. Bowden, *Appl. Phys. Lett.* **103**, 053511 (2013).
- ³⁹J. Schmidt, *Appl. Phys. Lett.* **82**, 2178 (2003).
- ⁴⁰J. Schmidt and R. A. Sinton, in *Proceedings of the 3rd World Conference on Photovoltaic Energy Conversion (WCPEC '03)*, Osaka, Japan (2003), pp. 947–950.
- ⁴¹B. G. Svensson, K. Rydén, and B. M. S. Lewerentz, *J. Appl. Phys.* **66**, 1699 (1989).
- ⁴²E. Olsen and E. J. Øvrelid, *Prog. Photovoltaics: Res. Appl.* **16**, 93 (2008).
- ⁴³T. U. Nærland, S. Bernardini, H. Haug, N. Stoddard, and M. Bertoni, in *Proceedings of the 43rd IEEE Photovoltaic Specialist Conference, Portland, USA* (2016), p. 62.
- ⁴⁴R. C. Newman, *J. Phys.: Condens. Matter* **12**, R335 (2000).
- ⁴⁵D. H. Macdonald, L. J. Geerligs, and A. Azzizi, *J. Appl. Phys.* **95**, 1021 (2004).
- ⁴⁶B. B. Paudyal, K. R. McIntosh, and D. H. Macdonald, in *34th IEEE Photovoltaic Specialists Conference, Philadelphia* (2009), p. 1588.
- ⁴⁷S. Rein, T. Rehl, W. Warta, and S. W. Glunz, *J. Appl. Phys.* **91**, 2059 (2002).
- ⁴⁸S. Bernardini, T. U. Nærland, A. L. Blum, G. Coletti, and M. I. Bertoni, *Prog. Photovoltaics: Res. Appl.* **25**, 209 (2017).
- ⁴⁹L. C. Kimerling and J. L. Benton, *Phys. B+C* **116**, 297 (1983).
- ⁵⁰J. E. Birkholz, K. Bothe, D. Macdonald, and J. Schmidt, *J. Appl. Phys.* **97**, 103708 (2005).
- ⁵¹A. Richter, F. Werner, A. Cuevas, J. Schmidt, and S. W. Glunz, *Energy Procedia* **27**, 88 (2012).
- ⁵²W. Shockley and W. T. Read, *Phys. Rev.* **87**, 835 (1952).
- ⁵³R. N. Hall, *Phys. Rev.* **87**, 387 (1952).
- ⁵⁴W. M. Bullis and H. R. Huff, *J. Electrochem. Soc.* **143**, 1399 (1996).
- ⁵⁵M. A. Green, *J. Appl. Phys.* **67**, 2944 (1990).